A geometric approach to modeling microstructurally small fatigue crack formation, part I: probabilistic simulation of constituent particle cracking in AA 7075-T651

J E Bozek[1], J D Hochhalter[1], M G Veilleux[1], M Liu[1], G Heber[1], S D Sintay[2], A D Rollett[2], D J Littlewood[3], A M Maniatty[3], H Weiland[4], R J Christ Jr.[5], J Payne[5], G Welsh[6], D G Harlow[7], P A Wawrzynek[1] and A R Ingraffea[1,8]

[1]Cornell Fracture Group, Cornell University, Ithaca, NY 14853
[2]Carnegie Mellon University, Pittsburgh, PA 15213
[3]Rensselaer Polytechnic Institute, Troy, NY 12180
[4]Alcoa Technical Center, Alcoa Center, PA 15069
[5]Northrop Grumman Integrated Systems, Technology Development, Bethpage, NY 11714
[6]United Technologies Research Center, East Hartford, CT 06108
[7]Lehigh University, Bethlehem, PA 18015

Abstract. Microstructurally small fatigue crack formation includes stages of incubation, nucleation, and microstructurally small propagation. In AA 7075-T651, the fracture of Al_7Cu_2Fe constituent particles is the major incubation source.. In experiments, it has been observed that only a small percentage of these Fe-bearing particles crack in a highly stressed volume. The work presented here addresses the identification of the particles prone to cracking and the prediction of particle cracking frequency, given a distribution of particles and crystallographic texture in such a volume. Three-dimensional elasto-viscoplastic finite element analyses are performed to develop a response surface for the tensile stress in the particle as a function of the strain level surrounding the particle, parent grain orientation, and particle aspect ratio. A technique for estimating particle strength from fracture toughness, particle size, and intrinsic flaw size is developed. Particle cracking is then determined by comparing particle stress and strength. The frequency of particle cracking is then predicted from sampling measured distributions of grain orientation, particle aspect ratio, and size. Good agreement is found between the predicted frequency of particle cracking and two preliminary validation experiments. An estimate of particle cracking frequency is important for simulating the next stages of microstructurally small fatigue crack formation: inserting all particles into a microstructural model for these stages is computationally intractable and physically unnecessary.

1. Introduction

The structural integrity of complex mechanical systems such as bridges, turbine engines and aircraft is a prime concern of engineering practice. Generous safety factors are often built into such systems in order to avoid catastrophic failure during use. In opposition, economic pressures, performance criteria, resource limitations and the desire for simplicity encourage efficient and elegant design. This issue is of particular importance when fatigue damage is a primary limitation of structural integrity and maximum utilization. Recent efforts to reduce the costs associated with overly conservative approaches to the avoidance of fatigue failure have emphasized the possibility of using specific knowledge of the fatigue process in conjunction with novel sensors and sophisticated reasoning techniques to create highly detailed, predictive models of fatigue damage (Christodoulou, 2004). This approach seeks to exploit thorough knowledge of the microstructural origins of fatigue failure combined with the power of modern computing to create high-fidelity physically-based models of the fatigue degradation process that can be used for probabilistic predictions of structural failure. As part of one such effort (Papazian, 2007a, 2007b), the microstructural origins of fatigue failure in commercial aluminum alloys are being codified

---

[8] Author to whom any correspondence should be addressed

into multi-scale, highly-detailed finite element models that are capable of analyzing the fatigue process in large complex systems while taking into account the specifics of the material microstructure. This paper addresses the first step in such a modeling capability, that of the incubation of cracks in aluminum alloy 7075-T651.

It is well known that, in the high-cycle regime, most of an aluminum alloy's fatigue life is spent in the microstructurally small fatigue crack (MSFC) formation phase. This phase consists of the crack incubation, nucleation, and microstructurally small propagation stages. Suresh (1998) asserted that up to 90% of the total fatigue life of a structural component could be consumed during the formation of a dominant fatigue crack. Other researchers have argued that the time spent before a crack becomes microstructurally large could be 50-70% of total fatigue life (Brockenbrough *et al.* 1994, Fan *et al.* 2001). McDowell *et al.* (2003) distinguished the distinct stages of MSFC formation and implemented a corresponding series of phenomenological models to predict the fatigue life in A356-T6. A complete understanding of the physical response and associated statistics, in each stage and proper sequence, of the microstructure during MSFC formation is still needed. One way to obtain additional insight is to couple improved experimental techniques with ever increasing computing power such that individual microcracks can be modeled directly, an explicitly geometrical approach. This strategy will provide an environment to explore the underlying physics and mechanics of the MSFC phase. The opportunity now exists to create and validate an improved prognosis capability, which accurately captures the stochastic behavior of this dominant fatigue life phase.

This is the first in a series of papers addressing such a capability, with aluminum alloy 7075-T651 as the proof-test material. Throughout this series, wherever possible, statistically accurate morphologies and textures are explicitly included in all three-dimensional FE models. The goal of this paper is to develop a microstructure-based model wherein the observed statistics related to incubation are accurately predicted. These incubation statistics are necessary inputs for statistically accurate simulations of the later stages of MSFC formation. Future papers will address these subsequent stages, nucleation and microstructurally small crack propagation, and provide validation of the implemented criteria and predicted statistics.

In general, incubation is the stage of MSFC formation that precedes and enables the development of new surface area in the alloy, and varies with alloy composition. In 7075-T651, a major element of the incubation process is the brittle cracking of Al_7Cu_2Fe constituent particles. This is a common observation in commercial aluminum alloys, which often contain such brittle intermetallic impurities (e.g. Morris 1976, Morris 1978, Kung 1979). Using optical and SEM microscopy to observe the notch root of a single edge-notch tension (SEN(T)) specimen, Gruenberg *et al.* (2003) conducted experiments to show that cracked particles serve as the origins of MSFC formation in 7075-T651. Other experimental results indicate that fatigue cracks in 7075-T651 are formed from the fractured Fe-bearing constituent particles located on the specimen surface (Xue *et al.* 2007). Some particles crack, while some particles debond from the matrix, but the debonded particles are much less effective in the nucleation of matrix cracks. Therefore, particle cracking is the dominant incubation mechanism of consequence in this alloy. Figures 1(a) and 1(b) are micrographs of a region surrounding a constituent particle after 3000 cycles of $R = 0$ constant amplitude loading at a far-field strain range of 1% in the rolling direction (RD). Figure 1(a), a SEM micrograph, shows the three phases of MSFC formation: (i) incubation, (ii) nucleation, and (iii) propagation. Generally, the crack is propagating on a plane defined by the normal direction (ND) and transverse direction (TD). Figure 1(b), an orientation imaging micrograph (OIM) shows the orientations of the surrounding grains in the aluminum matrix.

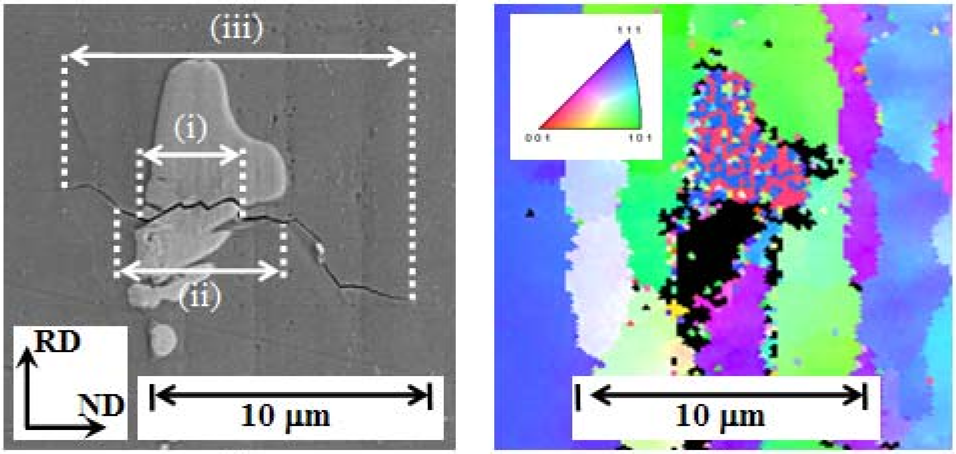

(a) (b)

Figure 1. Micrographs of an Al_7Cu_2Fe constituent particle on the surface of a fatigue loaded 7075-T651 rolled plate. (a) SEM micrograph showing regimes of (i) incubation, (ii) nucleation, and (iii) microstructurally short crack propagation, and (b) [001] inverse pole OIM image showing the surrounding grain structure.

In figure 2(a), many constituent particles (white) are observed embedded in the aluminum matrix. This SEM image was taken in a highly-stressed region with the sample under load, so that many fatigue cracks (black) can be observed. The larger field of view, figure 2(a), illustrates the stochastic nature of the fatigue phenomena at the microstructural scale. Under higher magnification, it is observed that most particles do not crack, figure 2(b), and of the few that do, figures 2(c) and 2(d), fewer nucleate a matrix crack and even fewer matrix cracks continue through MSFC propagation, figure 2(d).

From experimental observations, it has been hypothesized that particle aspect ratio and size, grain orientation, and strain level are the key parameters to explain the stochastic nature of particle cracking. In this paper, this hypothesis is tested using a combination of observations, measurements, and finite element (FE) analyses. The overall objective of this series of papers is to describe the development and validation of a computational simulation system capable of reproducing the mechanics and stochastic behavior of MSFC formation, as apparent in figure 2(a). A necessary first step is to answer quantitatively the question: Given a distribution of particles in a highly stressed area, which particles will crack? The answer to this question is important for simulating the next stages of MSFC formation: inserting all particles into a microstructural model for these stages is computationally intractable and physically unnecessary

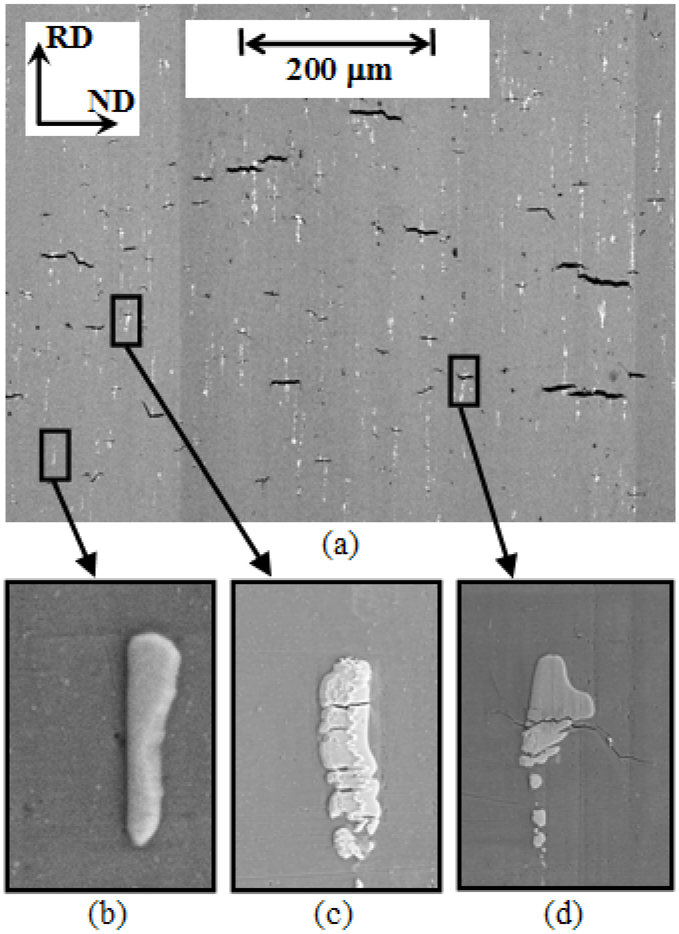

Figure 2. (a) SEM image of 7075-T651 under load, showing multiple, microstructurally small fatigue cracks. Close-up images show (b) an uncracked particle, (c) a cracked particle where the crack did not extend into the matrix, and (d) a cracked particle where the crack did extend into the matrix.

This paper is organized to answer this question systematically, and the strategy is depicted in figure 3. First, Section 2 contains a description of, and results from numerous finite element analyses performed on an idealized single grain/single surface particle model. The key variables studied are applied strain level, grain orientation, and particle aspect ratio. A response surface is then developed for a specific stress component at a particular point in the particle, σ_p. Next, a technique for determining a distribution of particle strength as a function of fracture toughness, K_{IC}, and particle size is described in Section 3. In Section 4, the results from Sections 2 and 3 are combined into a particle cracking criterion, charted in figure 3: a particle cracks if a measure of σ_p exceeds the particle strength, σ_{cr}. This criterion can be viewed as a filter or function dependent on distributions of particle aspect ratio, grain orientation, strain level surrounding the particle, particle size, particle fracture toughness, K_{IC}, and intrinsic flaw size, given by a material parameter, *C*, discussed in Section 3. This function is applied to observed particle distributions to predict particle cracking frequency. Section 5 presents a preliminary validation study of this criterion by comparing the predicted particle cracking frequency with experimental observations performed at Northrop Grumman Corporation. Section 6 summarizes observations and conclusions.

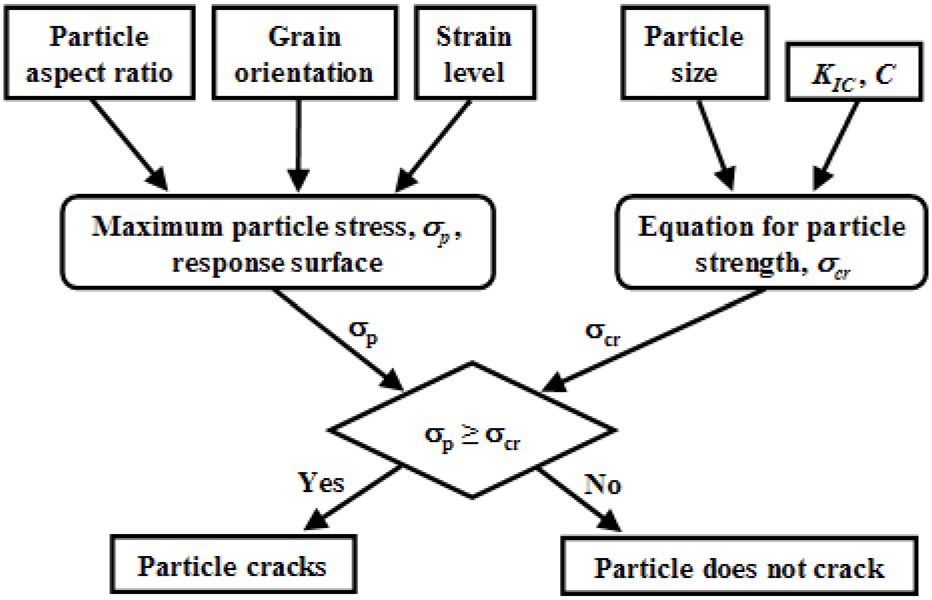

Figure 3. Flowchart of steps taken in this study to predict the frequency of particle cracking.

2. Methodology for generating a particle stress response surface

The objective of this section is to describe the development of a response surface from which the crack incubation driving force, i.e. tensile stress, can be determined for arbitrary particle configurations observed in 7075-T651. An extensive series of FE analyses is performed on a baseline model. Each analysis has a unique combination of three variables: grain orientation, particle aspect ratio, and applied strain level. Together, these FE analyses cover the breadth of these three variables for the material and load histories studied herein. The resulting particle tensile stresses from these analyses are consolidated into a response surface.

2.1. Finite element model: geometry, boundary conditions, and verification

The baseline structural model chosen for this study is an idealization of the interaction of a single particle with its surrounding matrix. As can be seen in figures 1 and 2, particle sizes and shapes are highly varied, as are their locations within grains. In a rolled 7075-T651 microstructure, constituent particles are elongated in the RD. Given the statistical objective of this study and initial hypotheses that absolute particle size and aspect ratio will be important geometrical variables, a simple shape that can account for these variables is desirable. Therefore, particle shape is idealized as ellipsoidal with the major axis aligned with the RD. It could be argued that such a simple particle geometry ignores the potential for higher stress amplification from irregular geometry, that is, such a simplification would skew the statistics by missing the particles most highly stressed because of local stress concentrations due to their geometry. However, all particles have some form of local stress concentrator, yet very few of them crack. Therefore, surmised, highly local stress concentration cannot be a statistically dominant influence. This is likely due to the diminution effect of highly local plastic deformation (Gao *et al.* 2004).

Further, in the baseline model, the idealized particle is on a RD-ND surface at a stress concentrating location. This location accounts for the fact that fatigue cracks most often begin at structure-scale geometric stress-risers. These produce gradients in local fields wherein highest values are most often on surfaces. Even in the absence of stress gradient influence, Mei and Morris (1993), for example, showed that, in an otherwise uniform stress field, inclusions experience higher stress on a free surface than in the interior.

Finally, in the baseline model, the idealized particle is centered on a RD-ND surface of a single grain, idealized as a cube. This simplification assumes that particles are very small compared to their containing grain, and that the statistics of particle cracking are dominated by intra-granular particles. Therefore, the baseline structural model is a semi-ellipsoidal surface particle in a cubic grain, figure 4. In the analyses to populate the response surface, the particle is modeled as a linear elastic, isotropic solid, and the grain as a rate-dependent, face-centered cubic (FCC) crystal plastic solid. This model has no inherent material length scale, so the absolute size of the baseline model is irrelevant and chosen for convenience. The constitutive model of the grain is detailed in Section 2.2.

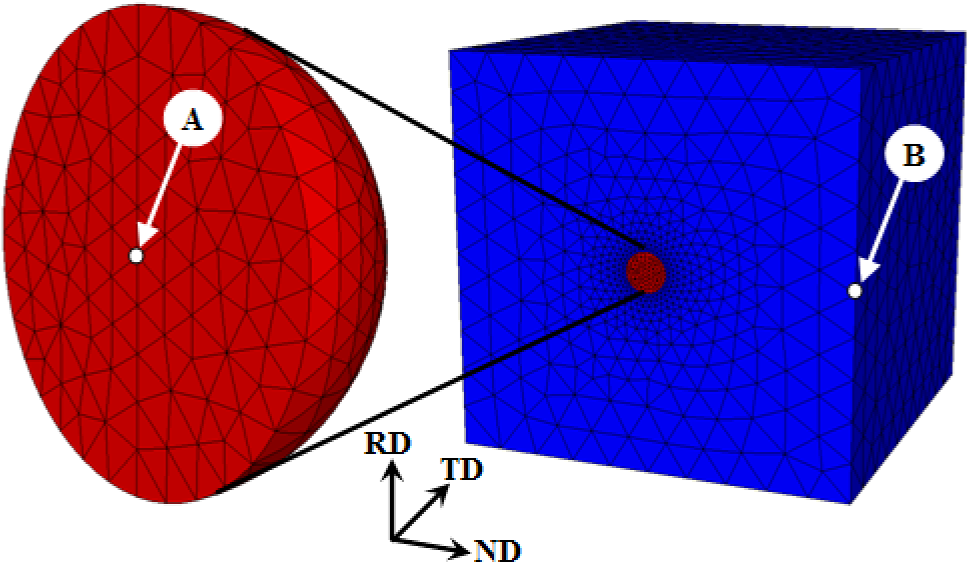

Figure 4. Typical surface mesh on an example baseline structural model.

The boundary conditions applied to the model are intended to emulate strain fields in a grain located on the surface at a notch tip of a double edge-notched (DEN) specimen. To obtain an accurate description of these strain fields, engineers at Northrop Grumman Corp. created an elasto-plastic FE model of a DEN specimen (Fridline 2007). The strain at the highly stressed notch tip was computed after applying cyclic load boundary conditions, figure 5, indicative of the experiment discussed later, in Section 5. A maximum notch strain of 1% in the RD with a corresponding R value of 0.07 was computed. Based on this analysis, displacement boundary conditions were applied to the surfaces of the baseline model such that the strain in the RD was 1%. Since the baseline model represents a grain embedded within a larger structure, the TD and ND components of strain in the baseline model are typically non-zero. Specifically, the out-of-plane boundary conditions on surfaces with normals in the TD or ND are between the two extremes of traction-free and fixed in the direction of the face normal. Thus, two sets of boundary conditions that represent these extremes envelope the actual conditions. In an initial sensitivity study, the RD normal tensile stress at point A in a particle, figure 4, was computed to be about 8% higher with the latter boundary conditions applied and particle aspect ratios RD:TD:ND = 11:3.5:3.5 for one particular grain orientation. At this time, it is unknown which boundary condition case better represents an embedded grain statistically. Therefore, all subsequent FE analyses used in the development of the response surface were conducted for both the unconstrained and constrained cases. Resulting differences in the particle cracking frequency, due to the two boundary conditions, are presented in Section 4.

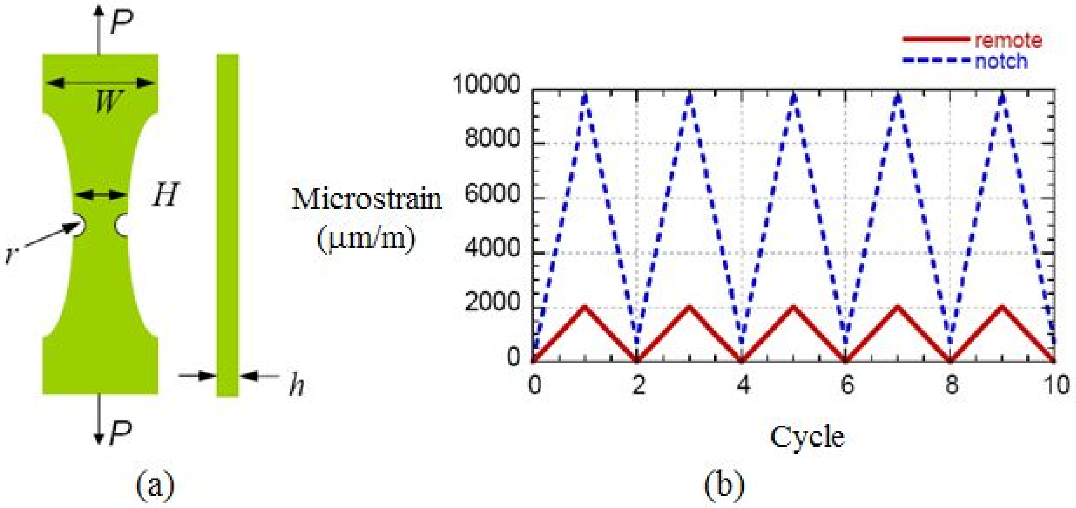

Figure 5. (a) Double edge notch specimen; W = 19 mm, H = 12.7 mm, r = 2.4 mm, h = 5.7 mm (b) Finite element computed notch strain and remotely applied cyclic loading. (Courtesy of Northrop Grumman Corp.)

Additional assumptions involved in the generation of the particle stress response surface using the baseline model are:

(i) Structural models are initially stress-free;
(ii) The particle and matrix are perfectly bonded, and;
(iii) Particle tensile stress is accurately obtained when only the influence of the surrounding grain is considered.

The first assumption is made because it is expected that the residual stresses are negligible when compared to the stresses induced by mechanical loading for hot-rolled materials. The second assumption is conservative, since any debonding would result in reduced tensile stress in the particle. The third assumption is the subject of an in-depth study which will be presented in a later publication.

A verification study was conducted to determine the level of finite element mesh refinement required in the response surface generation. Mei and Morris (1993) developed a semi-analytical technique for computing the stress field in and around ellipsoidal particles under conditions of linear elasticity for geometry and boundary conditions that are equivalent to the baseline model. To compare their semi-analytical solution with the present FE results, the baseline model was assigned linear elastic, isotropic material properties for both the grain and particle, where the particle elastic modulus was 3 times that of the grain, to match one of the solutions from Mei and Morris. The macroscopic elastic modulus of 7075-T651, 72 GPa, was assigned to the grain and, as a result, a modulus of 216 GPa was assigned to the particle. The particle was defined to be hemispherical, i.e. aspect ratio RD:TD:ND = 1:1:1. Also, following Mei and Morris, unit traction was applied uniaxially in the RD. The baseline model was then analyzed using 3 levels of mesh refinement: 6,000; 12,000, and; 25,000 degrees of freedom (dofs). The stress values were queried at a subsurface distance of 0.05 μm, following Mei and Morris. Figure 6, a plot of the RD stress components from point A to point B, figure 4(a), illustrates that with a minimum of

25,000 well-graded dofs, convergence of the FE computed stress to the analytical stress is acceptable. Mesh densities significantly greater than the finest level plotted in figure 6 were used in the FE analyses for response surface generation. A similar convergence study was performed for an additional baseline model with the FCC constitutive model for the grain. The difference in stress at Point A was less than 5% between FE models with about 10,000 and 100,000 dofs.

An in-house FE analysis code, Finite Element All Wheel Drive (FEAWD), was used to perform these analyses. The code has a parallel driver, which coordinates the partitioning, formulation, assembly, and solution of non-linear finite element equations. It is based on standard packages including MPI (Pacheco, 1997), ParMetis (Karypis *et al.* 2003), PETSc (Balay, *et al.* 2006), and the Cornell Fracture Group's FemLib library (Cornell Fracture Group 2007), which contains an implementation of the crystal plasticity model used during response surface generation. Ten-noded, hybrid, tetrahedral elements were used exclusively in all models.

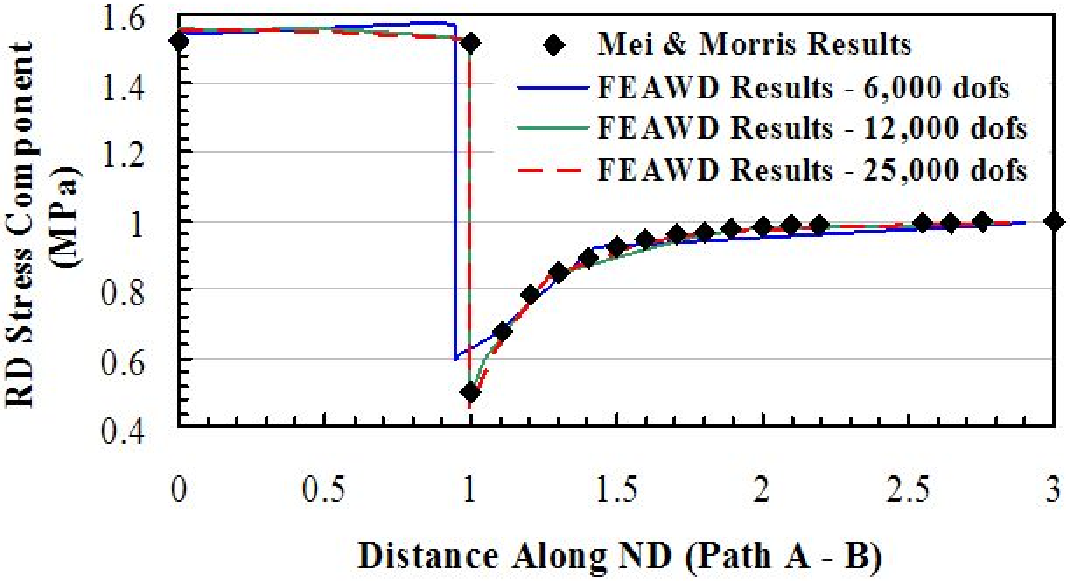

Figure 6. Mesh refinement verification results, comparing present FE results to a semi-analytical solution for a hemispherical surface inclusion in an infinite half-space (Mei and Morris 1993). Path A-B shown in Figure 4.

It was shown by Mei and Morris that the RD component of stress is nearly constant throughout a hemispherical surface particle (within 5%) when a linear elastic, isotropic model is applied to both the grain and particle. Because the particles considered here are significantly stiffer than the surrounding grain, the particle is subjected to higher stress. However, this is only necessarily true when the baseline model is undergoing linear elastic deformation, which is different than the FCC crystal plasticity model used to generate the response surface. In this latter case, depending on the surrounding grain's orientation, the particle can actually be relieved of stress after the onset of slip. For some orientations, this occurs because the grain loses its ability to transfer load to the particle. During loading, plastic slip first occurs along the particle-grain interface; the location on the interface where this first occurs is dependent on the surrounding grain's orientation. It can be expected that the orientation of the surrounding grain in the baseline model will affect the location of maximum stress in the particle. However, throughout the generation of the response surface, the RD component of particle stress was queried at point A, figure 4.

This was to stay consistent with observations that when particles crack, they tend to crack near the mid-plane, near point A.

2.2. Finite element model: constitutive behavior

The response of the 7075-T651 matrix material is governed by a crystal elasto-viscoplastic formulation that captures the relevant microstructural mechanisms. The overall formulation follows the work of Matous and Maniatty (2004) and is summarized here for completeness. At the grain scale, the deformation response to stress is assumed to follow a standard multiplicative decomposition, consisting of an elastic/lattice deformation and viscoplastic slip along crystallographic slip systems, which is accommodated by dislocation motion and is volume preserving (Lee, 1969). Summarizing,

$$\mathbf{F} = \mathbf{F}^{\mathbf{e}} \cdot \mathbf{F}^{\mathbf{p}} , \tag{1}$$

$$\det\left(\mathbf{F}^{p}\right) = 1 , \tag{2}$$

$$\mathbf{L} = \dot{\mathbf{F}}^{p} \cdot \mathbf{F}^{e^{-1}} + \mathbf{F}^{e} \cdot \hat{\mathbf{L}}^{p} \cdot \mathbf{F}^{e^{-1}} , \tag{3}$$

$$\hat{\mathbf{L}}^{p} = \dot{\mathbf{F}}^{p} \cdot \mathbf{F}^{p^{-1}} = \sum_{\alpha=1}^{N_s} \dot{\gamma}^{\alpha} \mathbf{P}^{\alpha} , \tag{4}$$

where $\mathbf{F}^{e}$ and $\mathbf{F}^{p}$ correspond to the elastic/lattice and plastic deformation gradients, respectively; $\mathbf{L}$ is the velocity gradient; $\hat{\mathbf{L}}^{\mathbf{p}}$ denotes the plastic velocity gradient on the relaxed, intermediate configuration; $\dot{\gamma}^{\alpha}$ is the rate of shearing on slip system α; N_s denotes the total number of slip systems; and $\mathbf{P}^{\alpha} = \mathbf{s}^{\alpha} \otimes \mathbf{m}^{\alpha}$ is the Schmid tensor. In addition, $\mathbf{s}^{\alpha}$ and $\mathbf{m}^{\alpha}$ are the slip direction and slip plane normal for the α slip system, respectively, and ⊗ indicates dyadic product. The twelve primary $\{111\}\langle 110\rangle$ slip systems for FCC crystals are considered here.

For the elastic response, a linear relationship, with cubic symmetry, is assumed between the second Piola-Kirchhoff stress, $\hat{\mathbf{S}}$, and the Green elastic strain, $\hat{\mathbf{E}}^{\mathbf{e}}$, on the relaxed configuration, which can be expressed as

$$\hat{\mathbf{S}} = \det\left(\mathbf{F}^{e}\right)\mathbf{F}^{e^{-1}} \boldsymbol{\sigma} \mathbf{F}^{e^{-T}} = \hat{\mathbf{C}} : \hat{\mathbf{E}}^{e} = 2\mu \hat{\mathbf{E}}^{e} + \lambda tr\left(\hat{\mathbf{E}}^{e}\right)\mathbf{I} - 2\eta \Xi : \hat{\mathbf{E}}^{e} , \tag{5}$$

$$\hat{\mathbf{E}}^{e} = \frac{1}{2}\left(\mathbf{F}^{e^{T}} \mathbf{F}^{e} - \mathbf{I}\right) , \tag{6}$$

where σ is the Cauchy stress, $\hat{\mathbf{C}}$ is the fourth order elasticity tensor, $\mathbf{I}$ is the second order identity tensor, and the fourth order tensor Ξ with respect to the lattice coordinates is simply

$$\Xi_{\hat{i}\hat{j}\hat{k}\hat{l}} = 1 , \qquad \text{if} \qquad \hat{i} = \hat{j} = \hat{k} = \hat{l} \text{ , or}$$

$$\Xi_{\hat{i}\hat{j}\hat{k}\hat{l}} = 0 \qquad \text{otherwise,} \tag{7}$$

where the hat indices indicate the lattice configuration, which may coincide with the relaxed configuration. The three elasticity parameters μ, λ, and η are related to the stiffness matrix elasticity coefficient as $\mu = \mathrm{C}_{44}$, $\lambda = \mathrm{C}_{12}$, and $2\eta = 2\mathrm{C}_{44} + \mathrm{C}_{12} - \mathrm{C}_{11}$.

For the plastic response, a power law relates the rate of shearing to the resolved shear stress, τ^{α}, on the on the α slip system,

$$\dot{\gamma}^{\alpha} = \dot{\gamma}_0 \frac{\tau^{\alpha}}{g^{\alpha}} \left| \frac{\tau^{\alpha}}{g^{\alpha}} \right|^{\frac{1}{m-1}}, \tag{8}$$

where $\dot{\gamma}_0$ is a reference shearing rate, m is the strain rate sensitivity, and g^{α} is the resistance to slip on the α slip system. The resolved shear stress on the α slip system can be related to the stress and elastic deformation through

$$\boldsymbol{\tau}^{\alpha} = \left(\mathbf{F}^{e^T} \mathbf{F}^{e} \hat{\mathbf{S}} \right) : \mathbf{P}^{\alpha}. \tag{9}$$

To complete the model, it remains to define the evolution of the resistance to slip, i.e. hardening, on the slip systems. 7075-T651 is a precipitation strengthened alloy, and the hardening is due to Orowan's (1947) mechanism of dispersion hardening. This mechanism is associated with dislocations bowing out between and forming loops about precipitates. The η' precipitates, which form as disks (thickness about 15 nm and diameter about 45 nm assumed here) on the {111} planes, are the primary strengthening phase (Li *et al.,* 1999). Hart (1972) proposed a model for dispersion hardening due to short range stresses for spherical precipitates and Mori and Tanaka (1973) proposed a model based on average internal stresses. For spherical precipitates, these models give similar predictions. More recently, models based on the Mori-Tanaka approach have been proposed in the context of crystal plasticity formulations (Schmitt *et al.*, 1997 and Han *et al.,* 2004). A model building on that developed in Schmitt *et al.* (1997), but that allows for saturation, is defined here. First, the resistance to slip, g^{α}, in Equation (9) is defined to evolve according to

$$\dot{g}^{\alpha} = G_0 \left(\frac{g_s - g^{\alpha}}{g_s - g_0} \right) \sum_{\beta=1}^{N_s} \mathbf{H}^{\alpha\beta} \left| \dot{\gamma}^{\beta} \right|, \tag{10}$$

where g_0 is the initial resistance to slip, g_s is the saturation value of g, G_0 is associated with the rate of hardening, and $\mathbf{H}^{\alpha\beta}$ is the slip interaction matrix that defines the relative strength of self and latent hardening on the slip systems. Here it is assumed that the hardening is due to internal stresses arising from the incompatibilities between the plastic strain field due to slip and the elastic precipitates. If one assumes that the elastic properties of the matrix are the same as those of the inclusion and approximate an inclusion as elliptical, then, using Eshelby's theory (Mura, 1987), the change in stress near the inclusion due to an increment in plastic deformation is

$$\boldsymbol{\Delta}\hat{\mathbf{S}} = \hat{\mathbf{C}} : (\Theta - \Phi) : (-\hat{\mathbf{D}}^{p} \Delta t), \tag{11}$$

where Θ is the Eshelby tensor, Φ is the fourth order identity tensor, $\hat{\mathbf{D}}^{\mathbf{p}}$ is the symmetric part of $\hat{\mathbf{L}}^{\mathbf{p}}$, and ($-\hat{\mathbf{D}}^{\mathbf{p}}\Delta t$) can be thought of as the eigenstrain in the precipitate. The assumption that the elastic properties of the matrix and inclusion are the same is a reasonable approximation since the η' precipitates are precursors to $MgZn_2$ η precipitates, and the elastic properties of $MgZn_2$ (hexagonal) and Al are relatively close. Assuming the precipitates form with equal likelihood on the four {111} planes, then the Eshelby tensor, Θ, can be taken as the average Eshelby tensor for these four cases. Now, computing the increment in resolved shear stress on the slip systems using Equation (9) and substituting the symmetric part of Equation (4) for $\hat{\mathbf{D}}^{\mathbf{p}}$, we obtain

$$\boldsymbol{\Delta\tau}^{\alpha} = \left(\mathbf{F}^{e^T}\mathbf{F}^{e}\right)\hat{\mathbf{C}} : \left[(\Phi - \Theta) : \sum_{\beta=1}^{N_s} \dot{\gamma}^{\beta}\mathbf{M}^{\beta}\Delta t\right] : \mathbf{P}^{\alpha}, \tag{12}$$

where $\mathbf{M}^{\boldsymbol{\beta}}$ is the symmetric part of $\mathbf{P}^{\beta}$. If one assumes the elastic deformations are small and neglect the higher order term, i.e. let $\mathbf{F}^{\mathbf{eT}}\mathbf{F}^{\mathbf{e}} \approx \mathbf{I}$, making use of the symmetry of $\hat{\mathbf{C}}$, and let this increment in stress be associated with the increase in hardening, then

$$\sum_{\beta=1}^{N_s} H^{\alpha\beta}\left|\dot{\gamma}^{\beta}\right| = \xi \sum_{\beta=1}^{N_s}\left|\mathbf{M}^{\alpha} : \left[\hat{\mathbf{C}} : (\Phi - \Theta)\right] : \mathbf{M}^{\beta}\right|\left|\dot{\gamma}^{\beta}\right|, \tag{13}$$

can be used to define $H^{\alpha,\beta}$, where ξ is a scalar coefficient that is defined to make the diagonal elements of $H^{\alpha,\beta}$ equal to one. The values for $H^{\alpha,\beta}$ along with the slip system numbering scheme used for reference are given in table 1.

Table 1. Hardening interaction matrix and slip system numbering.

slip system #	ID	1	2	3	4	5	6	7	8	9	10	11	12
$(111)[1\bar{1}0]$	1	1.0	0.50	0.50	0.50	0.59	0.088	0.088	0.50	0.59	0.18	0.088	0.088
$(111)[\bar{1}01]$	2	0.50	1.0	0.50	0.59	0.50	0.088	0.18	0.088	0.088	0.088	0.59	0.50
$(111)[01\bar{1}]$	3	0.50	0.50	1.0	0.088	0.088	0.18	0.088	0.59	0.50	0.088	0.50	0.59
$(\bar{1}11)[101]$	4	0.50	0.59	0.088	1.0	0.50	0.50	0.59	0.50	0.088	0.088	0.18	0.088
$(\bar{1}11)[\bar{1}\bar{1}0]$	5	0.59	0.50	0.088	0.50	1.0	0.50	0.088	0.088	0.18	0.59	0.088	0.50
$(\bar{1}11)[01\bar{1}]$	6	0.088	0.088	0.18	0.50	0.50	1.0	0.50	0.59	0.088	0.50	0.088	0.59
$(1\bar{1}1)[\bar{1}01]$	7	0.088	0.18	0.088	0.59	0.088	0.50	1.0	0.50	0.50	0.50	0.59	0.088
$(1\bar{1}1)[0\bar{1}\bar{1}]$	8	0.50	0.088	0.59	0.50	0.088	0.59	0.50	1.0	0.50	0.088	0.088	0.18
$(1\bar{1}1)[110]$	9	0.59	0.088	0.50	0.088	0.18	0.088	0.50	0.50	1.0	0.59	0.50	0.088
$(\bar{1}\bar{1}1)[\bar{1}10]$	10	0.18	0.088	0.088	0.088	0.59	0.50	0.50	0.088	0.59	1.0	0.50	0.50
$(\bar{1}\bar{1}1)[101]$	11	0.088	0.59	0.50	0.18	0.088	0.088	0.59	0.088	0.50	0.50	1.0	0.50
$(\bar{1}\bar{1}1)[0\bar{1}\bar{1}]$	12	0.088	0.50	0.59	0.088	0.50	0.59	0.088	0.18	0.088	0.50	0.50	1.0

The 7075-T651 constitutive model was calibrated against experimental data provided by Jordan *et al.* (2007). The FE model used for calibration was comprised of 299 hexahedral grains. The grains were constructed with an aspect ratio of RD:TD:ND=25:4:1, which approximates the observed aspect ratio of 50:4:1. The rolling dimension was reduced to facilitate the creation of a FE model with a sufficiently large number of grains. Grain orientations for the calibration model were assigned based on OIM measurements of 7075-T651. Material parameters are listed in table 2.

Table 2. Material parameters for 7075-T651.

m	0.005
g_0	220 MPa
$\dot{\gamma}_0$	1.0 s^{-1}
G_0	120 MPa
g_s	250 MPa
$\dot{\gamma}_s$	5.0 e^{10} s^{-1}
μ	28.3 GPa
λ	60.9 GPa
η	5.10 GPa

The mechanical properties of the particles were determined with an atomic force microscope (AFM) equipped with a nanoindenter. For the particles of interest, Al_7Cu_2Fe, a mean value of 160.9 GPa (standard deviation of 7.56 GPa) was measured for Young's modulus. This compares reasonably well to a slightly smaller mean value found by Oswald (2003). A Poisson's ratio of 0.3 was assumed.

2.3. Particle tensile stress under cyclic loading

This section addresses the evolution of particle tensile stress under cyclic loading. The load history studied here is constant amplitude, with a maximum notch strain of 1%, figure 5. The measured stress is σ_p, the RD tensile stress at point A in the particle, figure 4(a).

In figure 7, the evolution of σ_p during such cyclic loading of a typical model is shown. During the first half-cycle of loading, plastic flow occurs in the matrix adjacent to the particle. Upon unloading in the second half-cycle, the permanent deformations in the matrix cause a state of residual compression in the particle. During subsequent reloading, the residual compressive stress in the particle must be overcome before the particle experiences tensile stress. Therefore, the net tensile stress in the particle at the peak of second loading cycle is lower than that for the first cycle. Since the load history is constant amplitude, subsequent loading cycles do not lead to an increase in σ_p.

Based on these results, all models used in the generation of the response surface were subjected to 1% monotonic strain. This simplification implies that, if particles crack, they do so in the first loading cycle. This is in agreement with experimental observations, which have shown that about 50-85% of all particles that are going to crack, do so in the first load cycle, as discussed in Section 5.

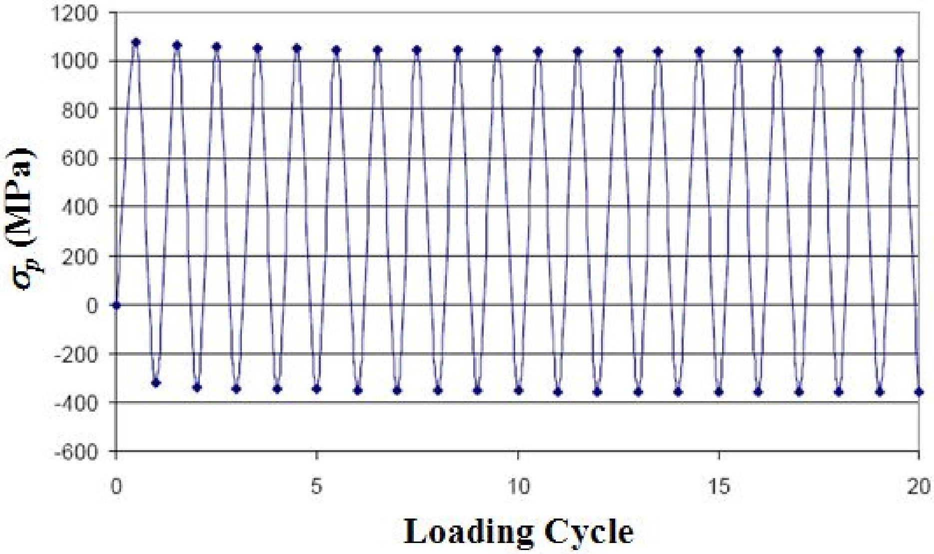

Figure 7. Computed σ_p vs. loading cycles for a typical single grain/single particle model under constant amplitude loading with a maximum strain of 1% and an R value of 0.07.

2.4. Creating the particle tensile stress response surface

To populate the particle tensile stress response surface, 1296 finite element analyses were conducted for each of the two boundary conditions considered, where each analysis corresponds to a specific combination of grain orientation, particle aspect ratio, and applied strain level. Lagrange interpolation functions were used to create a response surface from which σ_p can be interpolated given any arbitrary combination of these 3 variables. In this section, the dependence of the response surface on each individual variable and the functions used for interpolation between the stored results are discussed.

2.4.1. Dependence of particle tensile stress on grain orientation

Grain orientation is represented here as a Rodrigues vector, ($r1, r2, r3$). The Rodrigues space extends to infinity, but for crystals possessing sufficient symmetries, any orientation can be represented by its symmetric equivalent near the origin. For FCC crystals, the fundamental region of the underlying symmetry group is a truncated cube in Rodrigues space (Heinz and Neumann 1993), figure 8(a). The six cube face centers of this FCC fundamental region are a distance of $\sqrt{2}-1$ from the origin, while the eight planes truncating the corners of the cube are $1/\sqrt[3]{3}$ from the origin.

The FCC fundamental region was discretized into 444 linear tetrahedral elements with 144 vertices. The surface mesh for this discretization is shown in figure 8(b). Each vertex in this discretization corresponds to a modeled grain orientation. For each modeled grain orientation, σ_p was computed using the model discussed in Sections 2.1-3.

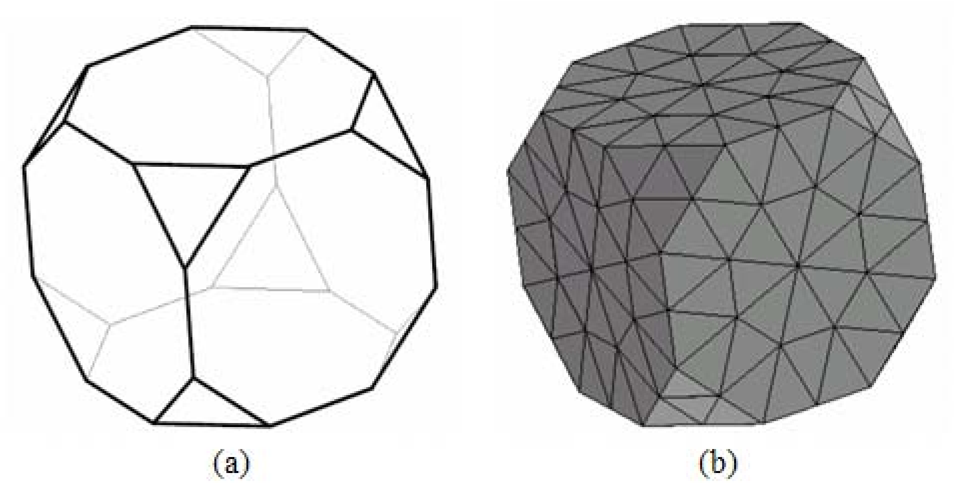
(a)
(b)

Figure 8. (a) Fundamental region for FCC symmetry in of Rodrigues space. (b) Finite element discretization of the fundamental region with 444 linear tetrahedral elements and 144 vertices.

The computed dependence of σ_p on grain orientation can be visualized by color contouring the FCC fundamental region. The σ_p distribution for a particle aspect ratio of RD:TD:ND = 11:3.5:1, unconstrained boundary conditions, and an applied strain of 1% is shown in figure 9. Since the microstructural anisotropy is taken into account in the material model, an anisotropic response is observed. It is clearly seen that grain orientation affects σ_p significantly: the maximum computed stress is about 30% higher than the minimum. In general, σ_p for the constrained boundary condition was 20 to 30% higher than for the corresponding orientation with the unconstrained boundary condition. This is to be expected because, under constrained boundary conditions, a higher stress is needed in the RD direction for the same level of applied strain in that direction. For a simple case of uniform geometry and linear elastic response, one would expect the increase in stress to be in direct proportion to Poisson's ratio. For the present case, with a variable geometry hard inclusion and elasto-crystal-plastic response, the observed increase in σ_p is reasonable. For use in the next two sections, three characteristic grain orientations are selected from those analyzed. These are denoted the high, intermediate, and low stress orientations. The corresponding orientation parameters and σ_p values are given in table 3.

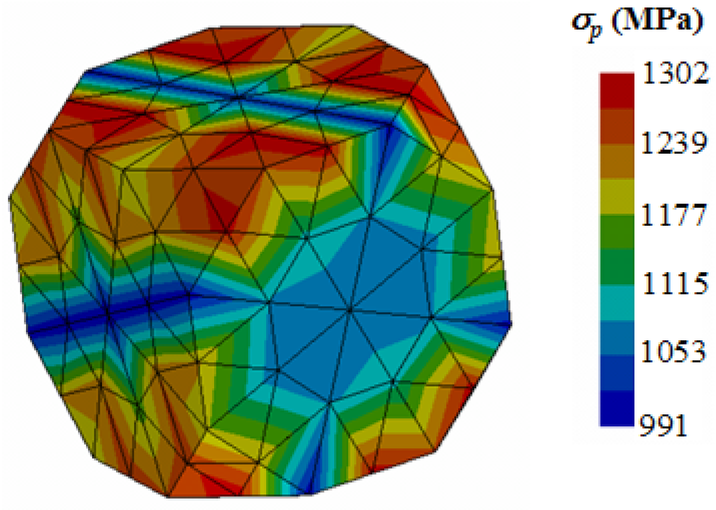

Figure 9. Computed σ_p in FCC fundamental region with a particle aspect ratio of RD:TD:ND = 11:3.5:1 and an applied strain of 1%, unconstrained boundary conditions.

Table 3. Computed results for three sample characteristic orientations for the unconstrained baseline model with a particle aspect ratio of RD:TD:ND = 11:3.5:1 and an applied strain of 1%.

Orientation label	Rodrigues parameters (*r1, r2, r3*)	σ_p (MPa)
High stress	(-0.2071, 0.4142, -0.0858)	1302
Intermediate stress	(0.0858, 0.2071, -0.2071)	1180
Low stress	(0.0, 0.0, -0.4142)	991

2.4.2. Dependence of σ_p on aspect ratio

In this section, the relationship between σ_p and particle aspect ratio is investigated. Since results for each of the 144 orientations cannot be shown here, the 3 characteristic orientations given in table 3 are considered. During an initial investigation, RD:ND, RD:TD, and TD:ND aspect ratios of the ellipsoidal particles ranging from 1:1 to 10:1 , 2:1 to 10:1, and 1:1 to 5:1, respectively, were modeled. The computed dependence of σ_p on the particle aspect ratios, for the unconstrained boundary condition, is shown in figure 10. Similar results were experienced for the constrained boundary condition. The computed σ_p increases as the RD:ND and RD:TD aspect ratios increase, and as the TD:ND aspect ratio decreases. The independent effect of particle aspect ratio on stress can account for a maximum σ_p 100% greater than the minimum for a given orientation. The combined effect of both the grain orientation and the particle aspect ratio on the tensile stress can produce differences of nearly 200%.

Based on these preliminary studies, it was found that σ_p behaves approximately quadratically as a function of each aspect ratio. For this reason, the σ_p response surface was populated using 9 different aspect ratios, enough for quadratic interpolation as discussed in Section 2.4.4.

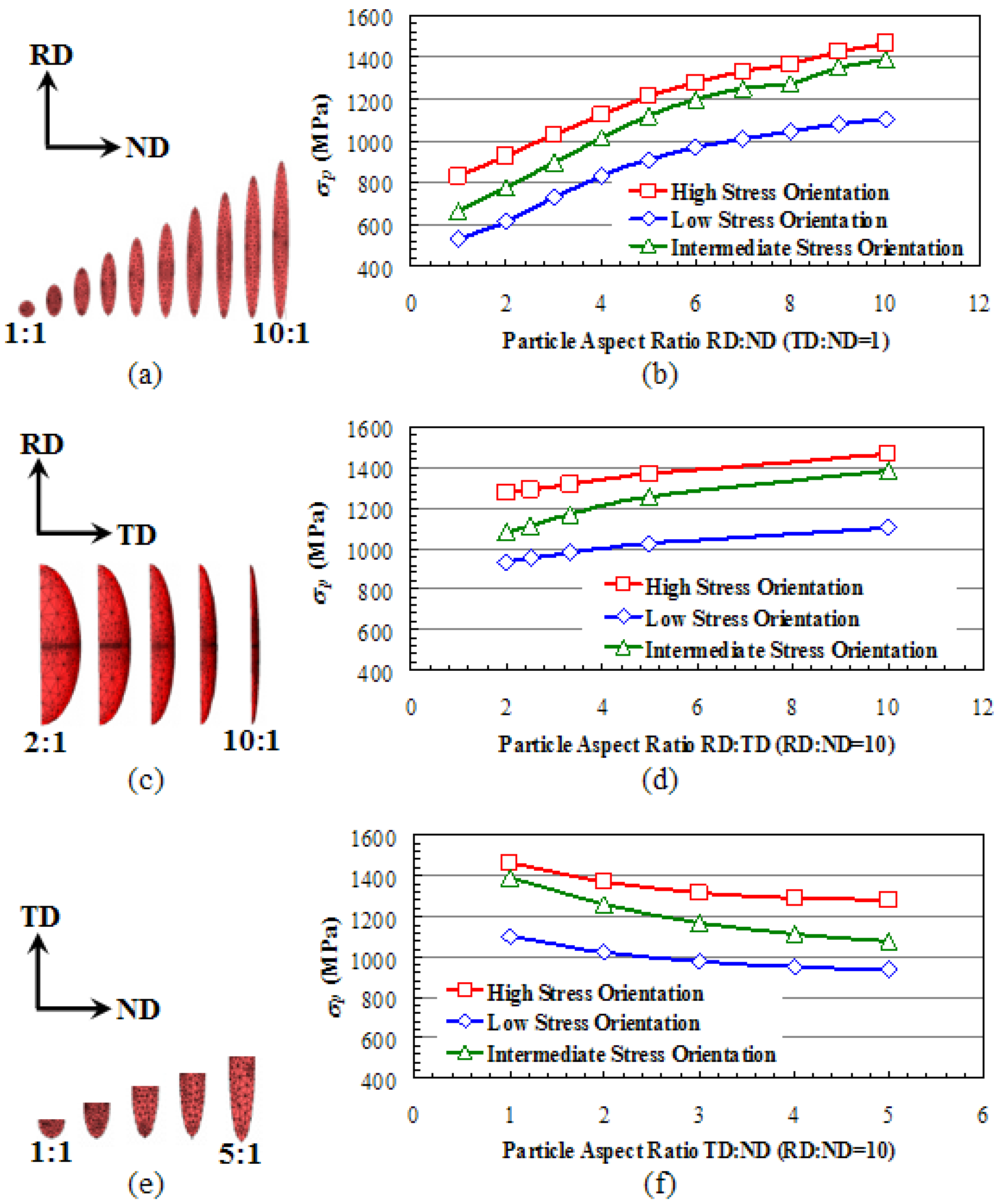

Figure 10. (a) Variation of particle aspect ratio, RD:ND (TD:ND = 1); (b) Dependence of σ_p on particle aspect ratio RD:ND, which is chosen equal to RD:TD, and grain orientation; (c) Variation of particle aspect ratio, RD:TD (RD:ND = 10:1); (d) Dependence of σ_p on particle aspect ratio RD:TD and grain orientation; (e) Variation of particle aspect ratio, TD:ND (RD:ND = 10:1); (f) Dependence of σ_p on particle aspect ratio TD:ND and grain orientation. Unconstrained boundary conditions.

2.4.3. Dependence of σ_p on applied strain level

In addition to grain orientation and particle aspect ratio, the applied strain level is another key parameter in determining σ_p. Let the particle aspect ratio be fixed at RD:TD:ND = 11:3.5:1 and consider the three characteristic orientations introduced in table 3. As the applied strain level is monotonically increased, a nearly bi-linear response in σ_p is computed, figure 11. The results suggest that σ_p remains almost constant after the elasto-plastic transition for the low stress case but increases at almost the elastic slope for the high stress case. The transition point corresponds to the initiation of plastic slip in the grain. The relationship between σ_p and applied strain, ε_{app}, can be written as

$$\sigma_p = \frac{\sigma_T}{\varepsilon_T}\varepsilon_{app}, \varepsilon_{app} < \varepsilon_T ,$$

$$\sigma_p = k(\varepsilon_{app} - \varepsilon_T) + \sigma_T , \varepsilon_{app} \geq \varepsilon_T , \tag{14}$$

where (ε_T, σ_T) represents the transition point and k denotes the slope after the transition, figure 12.

Note that for a given combination of grain orientation and particle aspect ratio, σ_p can be approximated as a function of ε_{app} using equation (14). This provides the basis for the stress response surface discussed in the following section.

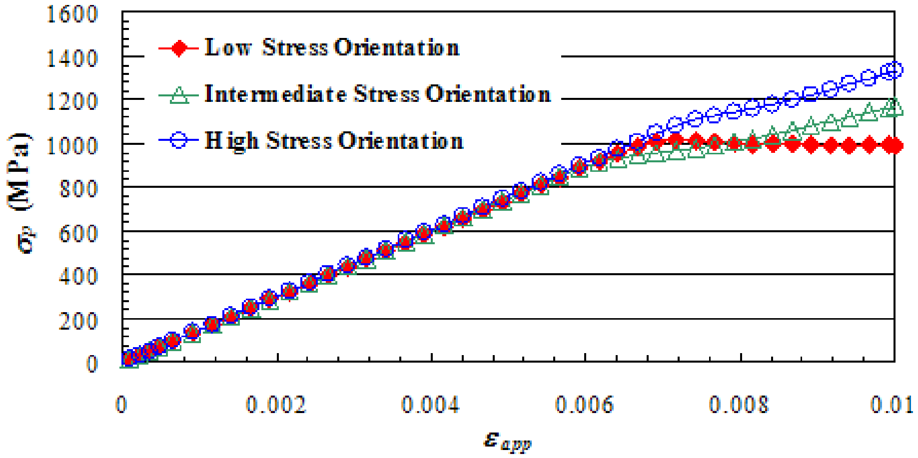

Figure 11. Example computed σ_p vs. ε_{app}. Particle aspect ratios RD:ND = 11:1 and TD:ND = 3.5 :1. Unconstrained boundary conditions.

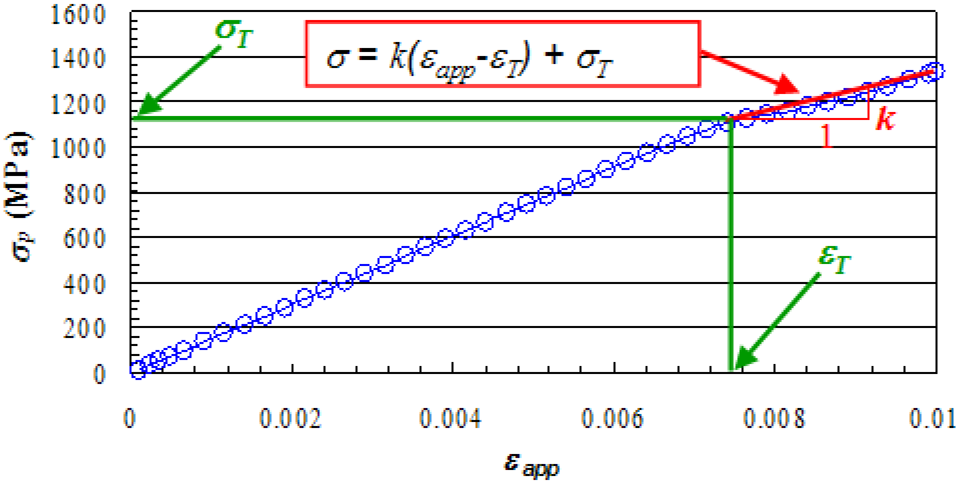

Figure 12. Piecewise linear approximation between σ_p and ε_{app}. Unconstrained boundary conditions.

2.4.4. Response surface for σ_p

A response surface for σ_p is created as a two-stage interpolation scheme using standard FE interpolation. The interpolation is performed first in orientation space and then in aspect ratio space. Using the information described in Sections 2.4.1-3, the response surface captures the dependence of σ_p on grain orientation, particle aspect ratio, and ε_{app}.

A total of 1296 separate FE simulations were performed to populate the response surface for each of the two boundary conditions considered. This consisted of 144 grain orientations performed on each of the 9 particle aspect ratios considered. Each individual analysis resulted in an approximately bi-linear stress-strain relationship, Equation (14). The FE interpolation in orientation space is performed on the finite element mesh of the fundamental region, figure 8(b), while the interpolation in aspect ratio space is performed on a nine-noded quadrilateral (Q9), figure 13. The Q9 was chosen to represent the quadratic relationship between σ_p and aspect ratio, as previously discussed in Section 2.4.2.

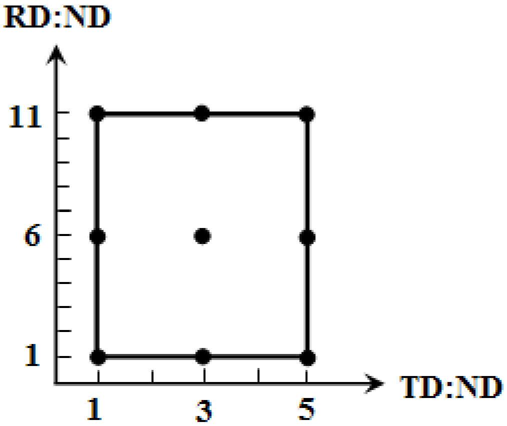

Figure 13. Nine-noded quadratic quadrilateral element used to interpolate σ_p for particle aspect ratio (RD:ND, TD:ND).

The use of the response surface can be summarized in the following manner. Given an arbitrary set of inputs of applied strain level, ε_{app}, grain orientation, *R*, and particle aspect ratio, *AR*, σ_p is determined as follows:

(i) Locate the tetrahedral element, *T*, in the FCC fundamental region mesh, figure 8(b), which contains *R*;
(ii) Determine the four corner nodes of *T*;
(iii) Obtain the stress at each corner node using ε_{app} and equation (14);
(iv) Interpolate stress values using the shape functions of *T* and *R*:

$$\sigma_j = \sum_{i=1}^{4} N_i(R)\sigma_i \qquad (15)$$

(v) Repeat steps (i) through (iv) for the nine different aspect ratio values, populating the nine nodes shown in figure 13;
(vi) Finally, interpolate σ_p using the Q9 shape functions and *AR*:

$$\sigma_p = \sum_{j=1}^{9} \Phi_j(AR)\sigma_j \tag{16}$$

where $N_i(R)$ are the standard four-noded tetrahedral element shape functions and $\Phi_j(AR)$ are the standard Q9 shape functions.

A methodology for computing σ_p in an ellipsoidal particle has now been presented. To complete the criterion for particle cracking, given a particle in a distribution of particles, the particle strength must also be known. The following section details the process and assumptions of predicting the particle strength, which results from both experimentation and LEFM calculation.

3. Estimation of particle tensile strength

Direct measurements of Al_7Cu_2Fe particle strength are not available to the best knowledge of the authors. Therefore, this section describes a technique for estimating particle strength, σ_{cr}. The following assumptions are made:

(i) If a particle cracks, it does so in the first half-cycle of loading;
(ii) σ_{cr} is a function of particle size, due to the presence of inherent particle flaws;
(iii) An inherent surface flaw exists that lies perpendicular to RD, figure 14;
(iv) The inherent flaw size is much smaller than the particle size;
(v) The shape of this inherent flaw is semi-elliptical, figure 14;
(vi) a_f *and* b_f are proportional to a_p and b_p; and,
(vii) LEFM conditions apply.

As stated in Section 2, assumption (i) is supported by experimental observation. Assumption (ii) has been commonly used in previous works (Murakami and Endo 1994, Curtin 1994). The flaw is assumed to be oriented perpendicular to the direction of maximum tensile stress, assumption (iii), because this is the orientation that yields the highest Mode I stress intensity factor. Assumption (iv), that $a_f << a_p$, is supported by Ghosh and Moorthy (1998). Furthermore, since these flaws are undetectable at the microstructural scale, their actual shape and size is unknown. Thus, for simplicity, the flaw shape is assumed to be semi-elliptical and a_f and b_f are assumed to be proportional to a_p and b_p, assumptions (v) and (vi), respectively. Specifically, the proportionality assumption can be expressed as:

$$a_f = Ca_p,\ b_f = Cb_p \tag{17}$$

where C is a material dependent parameter. Finally, assumption (vii) was made because the particles are in a brittle state, with a measured very low toughness. Since LEFM conditions, a semi-elliptical shape, and C<<1 are assumed, the initial flaw configuration, figure 14, can be approximated as a semi-elliptical surface crack in an infinite plate with a well known critical Mode I stress intensity factor solution (Raju and Newman 1979),

$$K_{IC} = \sigma_{cr}\sqrt{\pi\, F(a_f, b_f)}\ . \tag{18}$$

Solving (18) for σ_{cr} and substituting (17) into (18) yields the strength equation used herein,

$$\sigma_{cr} = \frac{K_{IC}}{\sqrt{\pi\, F(a_f, b_f)}} = \frac{K_{IC}}{\sqrt{\pi\, C\, F(a_p, b_p)}}\ . \tag{19}$$

As indicated in Section 4.2, a distribution of σ_{cr} can be calculated given distributions of K_{IC}, C, a_p, and b_p. Values of K_{IC} for twelve Al_7Cu_2Fe second-phase particles were estimated from a Vickers hardness test with a nano-indenter following the procedure established by Lawn (1993). The mean value of K_{IC} was determined to be 0.14 MPa√m with a standard deviation of 0.07 MPa√m. Figure 15 shows the relationship among σ_{cr}, a_p, and C for K_{IC} = 0.14 MPa√m. Specifically, for all values of C, the strength decreases as particle size increases; therefore, larger particles are more likely to crack than smaller particles. This is consistent with observations (Brockenbrough, *et al.* 1994, and Gruenberg, *et al.* 1999). Thus, two questions remain: Is C a material dependent parameter? And, if so, what is the range of C values for Al_7Cu_2Fe? A preliminary answer to the latter question is given in the following section.

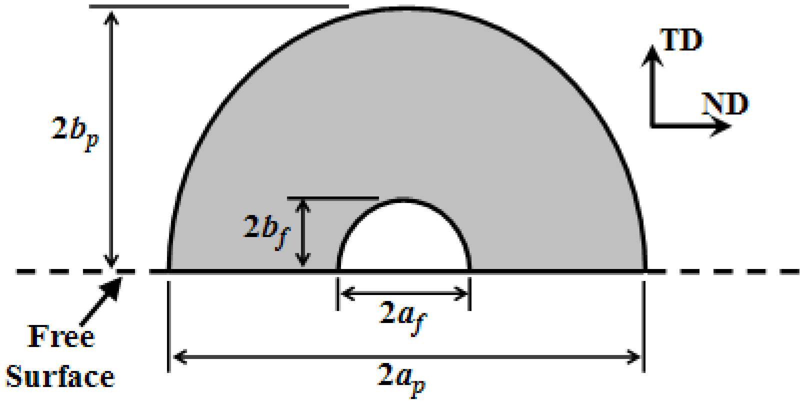

Figure 14. Cross-section of a semi-elliptical surface particle, with major and minor radii, a_p and b_p, containing a pre-existing, semi-elliptical surface crack, with major and minor radii, a_f and b_f.

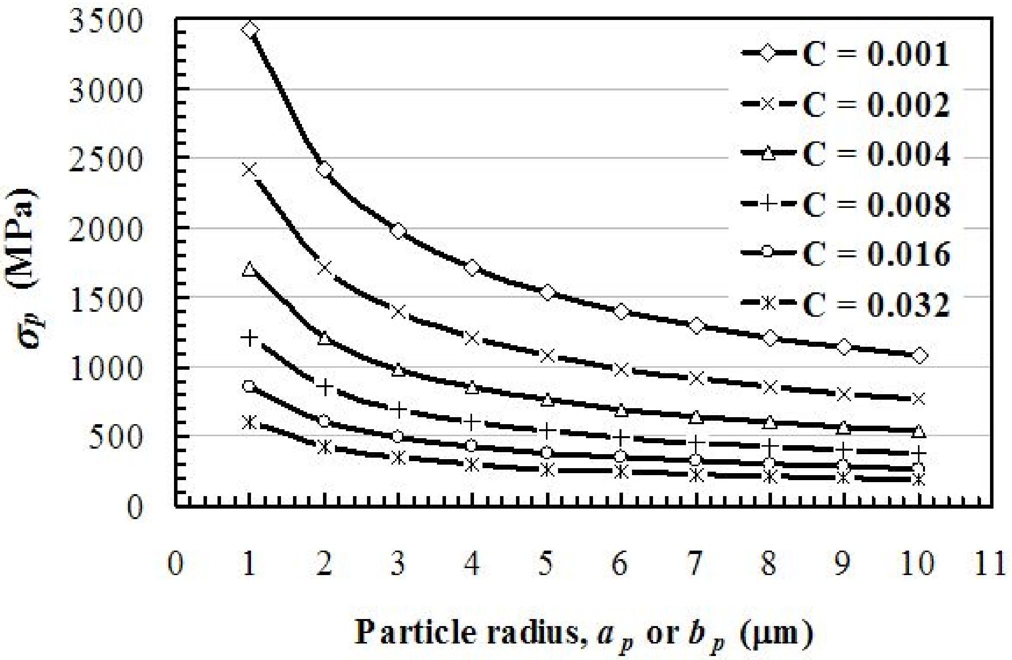

Figure 15. Particle tensile strength, σ_{cr}, vs. particle radius, a_p, for K_{IC} = 0.14 MPa√m.

3.1. Calibration of the particle tensile strength parameter, C

The material parameter, *C*, was calibrated for one microstructure sample, figure 16(a), with a single cracked particle, observed on the surface at a notch tip of a DEN specimen. For this sample, the experimentally recorded local texture, microstructure geometry, and applied strain at the time of particle cracking were replicated in a FE model, figure 16(b). The model size is that of the observation area, 50 μm in the RD and 30 μm in the ND. The microstructure was not observed in the third dimension, the TD. Therefore, a 2.5-dimensional replication model was created: the geometry was extruded 7 μm in the TD and all grains were assigned the orientations observed on the free surface. Observations of the microstructure were made only prior to and after the first half-cycle, and it was found in the latter observation that the particle had cracked. Thus, it was assumed that the particle cracked at full load, 1% strain in the RD. The boundary conditions for the replication model were identical to those discussed in the baseline model, for both the constrained and unconstrained cases. The constitutive models applied to the particle and grains are those described in Section 2.2. For the resulting finite element model, a mesh convergence study was run for the two boundary conditions considered, figure 17. Three meshes (0.7 million dofs, 1.3 million dofs, and 4.2 million dofs) were run for each of the two boundary conditions.

The maximum particle stress for the two boundary conditions was computed to be located at point P, figures 16(b) and 17. The stress found here for the most refined mesh, 1583 MPa and 1351 MPa for the constrained and unconstrained boundary conditions, respectively, is the assumed σ_{cr} for this particle. If $2a_p$ = 3.48 μm is taken to be the particle diameter on the free surface, figure 16(a), then the value of a_p is 1.74 μm. By using these values for σ_{cr} and a_p, and a mean K_{IC} of 0.14 MPa√m with a standard deviation of 0.07 MPa√m, and assuming semi-circular shape crack, Equation (19) was solved for *C* to get corresponding values: 0.0027 with a standard deviation of 0.0013 for the constrained case, and 0.0037 with a standard deviation of 0.0018 for the unconstrained boundary condition. Obviously, the value of C depends on the boundary condition applied because the parameter is being calibrated for only a single microstructural sample. This difference in C values will result in a corresponding difference in predicted particle cracking frequency, as discussed in the next section.

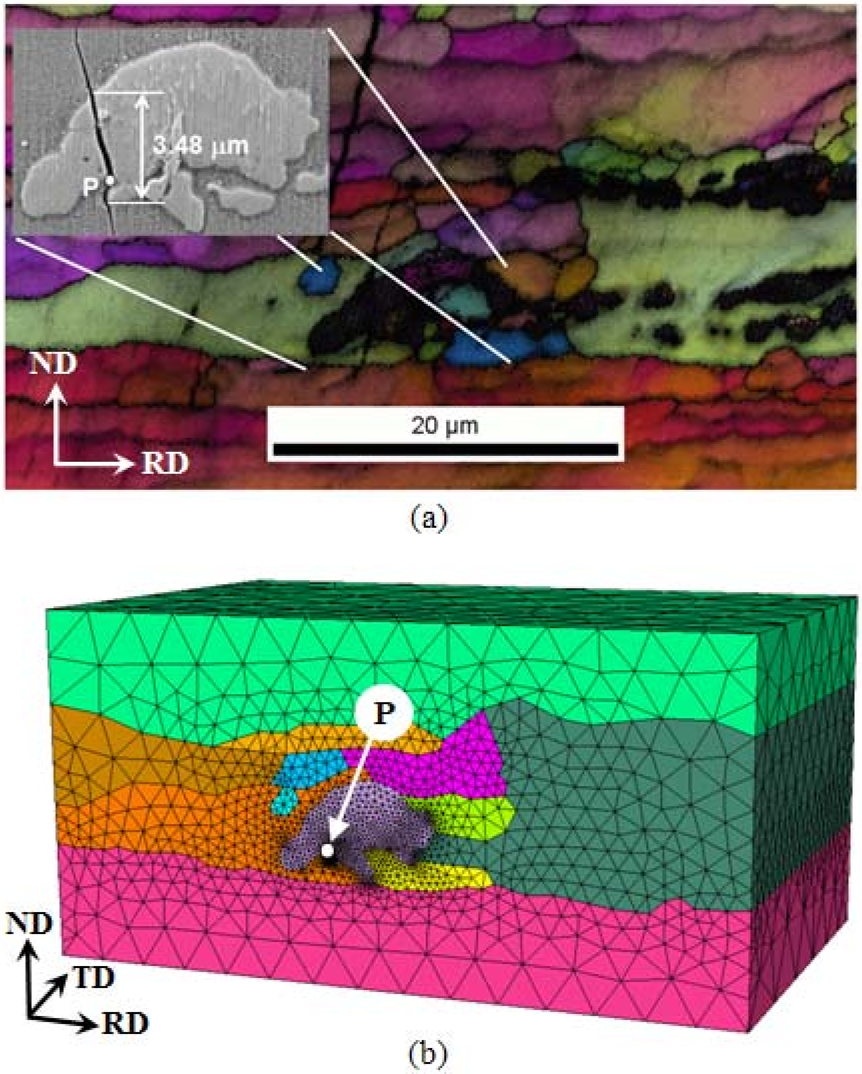

(a)

(b)

Figure 16. (a) SEM/OIM image of a 7075-T651 microstructure on the RD-ND free surface. (Courtesy of Northrop Grumman Corp.) (b) Finite element mesh for the replication model, where colors indicate unique regions: grains and a particle.

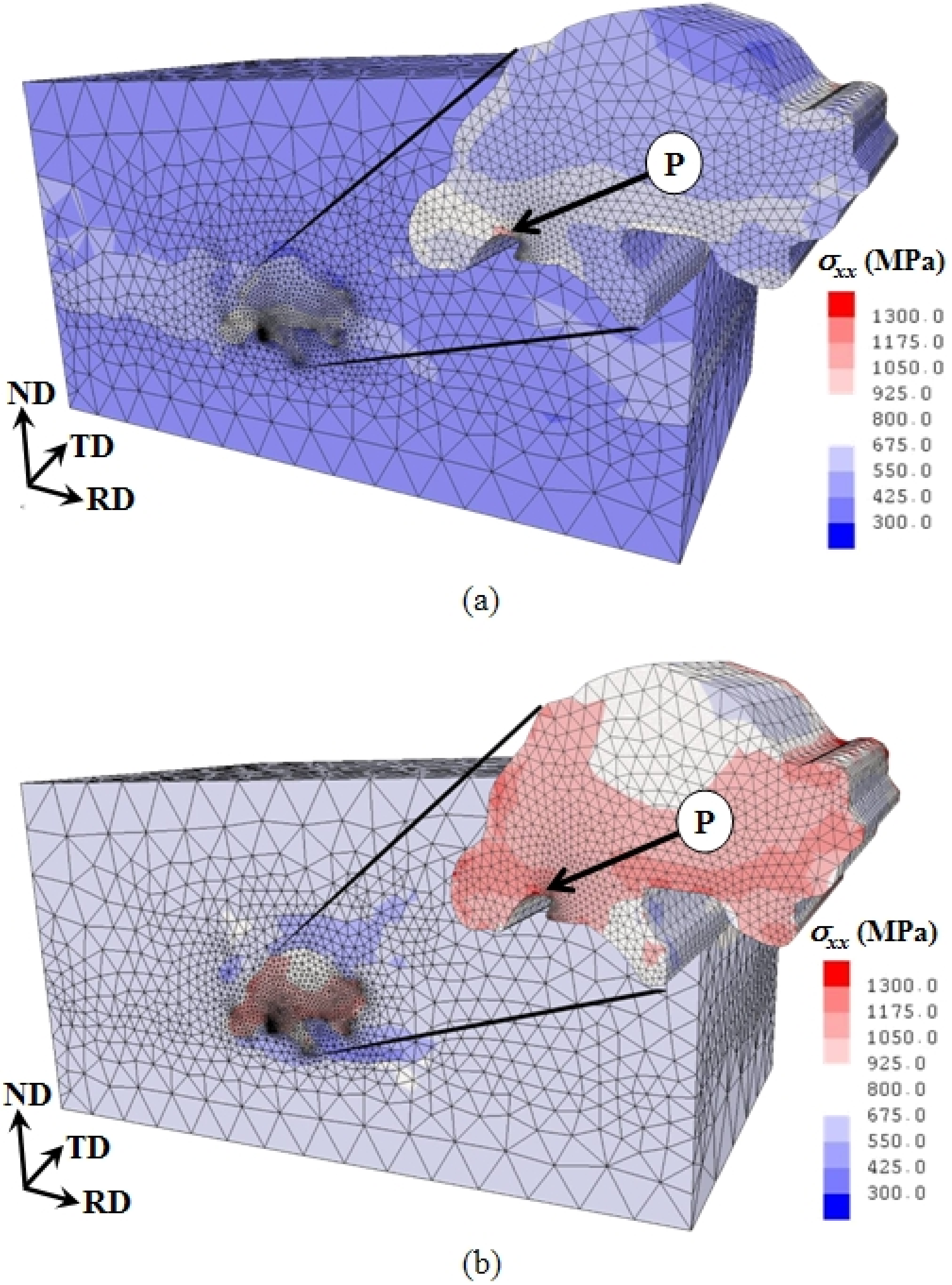

Figure 17. (a) Tensile stress, σ_{RD}, plot for a coarse mesh for the unconstrained boundary condition (b) Tensile stress, σ_{RD}, plot for a coarse mesh for the constrained boundary condition.

The relationship shown in figure 15 governs only the statistical resistance side of the particle cracking criterion. An input to figure 15 with a value of C and a measured distribution of a_p and b_p values produces an output distribution of σ_{cr} values. However, it has been shown in Section 2 of this paper that texture, aspect ratio and strain level govern the statistical driving force side of the equation: a large particle with a large inherent flaw might find itself in a relatively low tensile stress state and not crack. The process for comparing these distributions of strength and stress is presented in the next section.

4. Prediction of particle cracking frequency

In this section, a method for predicting cracking of both individual particles and distributions of particles is discussed. The particle cracking prediction utilizes both the particle tensile stress response surface, Section 2, and the estimation of particle strength, Section 3. The predicted frequency of particle cracking is compared with the experimentally observed frequency in Section 5.

4.1. Predicting cracking of a single particle

Particle cracking is governed by a comparison of the RD tensile stress at point A in the particle, σ_p, with the particle strength σ_{cr}; if the former exceeds the latter, the particle will crack. The process for determining whether a particle cracks is shown schematically in figure 3. The input variables include applied strain level, grain orientation, particle aspect ratio, particle size, particle fracture toughness, and the material inherent flaw size parameter, *C*. The procedure can be summarized as follows:

(i) Use the stress response surface to interpolate σ_p from the input applied strain level, grain orientation, and particle aspect ratio;
(ii) Use equation (19) to evaluate σ_{cr} from the input variables of particle size, particle fracture toughness, and *C*;
(iii) Predict particle cracking if $\sigma_p \geq \sigma_{cr}$.

4.2. Estimating the frequency of particle cracking

Different volumes of 7075-T651 undergoing the same processing steps exhibit statistical variability in microstructural features. This variability affects the material performance directly, causing scatter in both σ_p and σ_{cr} for individual particles.

The process described in Section 4.1 provides a link between the statistical variability of microstructural features and the probability of particle cracking. This process can be viewed as a function, which can be evaluated on measured distributions of particle size and aspect ratio, and grain orientation to obtain the frequency of particle cracking.

Based on known distributions for particle size, aspect ratio, and texture (Campman 2005, Harlow *et al.* 2006, Rollett 2006), several statistically accurate realizations were generated, each of which contained 10,000 particles and grain orientations. The observation of particle sizes was experimentally limited to particles with area, in the RD-ND plane, greater than 6 $\mu\mathrm{m}^2$; therefore, this paper does not consider particles with areas less than 6 $\mu\mathrm{m}^2$. The applied strain was fixed at 1%, the fracture toughness at $0.14\,\mathrm{MPa}\sqrt{\mathrm{m}}$, and C at 0.0037, the mean value computed for the unconstrained boundary conditions. The particle cracking frequency is defined as follows:

$$\text{particle cracking frequency} = \frac{\text{number of cracked particles}}{\text{total number of particles}} \tag{20}$$

Figure 18 shows the resulting histograms for $\sigma_{p,}$ based on unconstrained boundary conditions, and σ_{cr} for one such 10,000 particle realization.

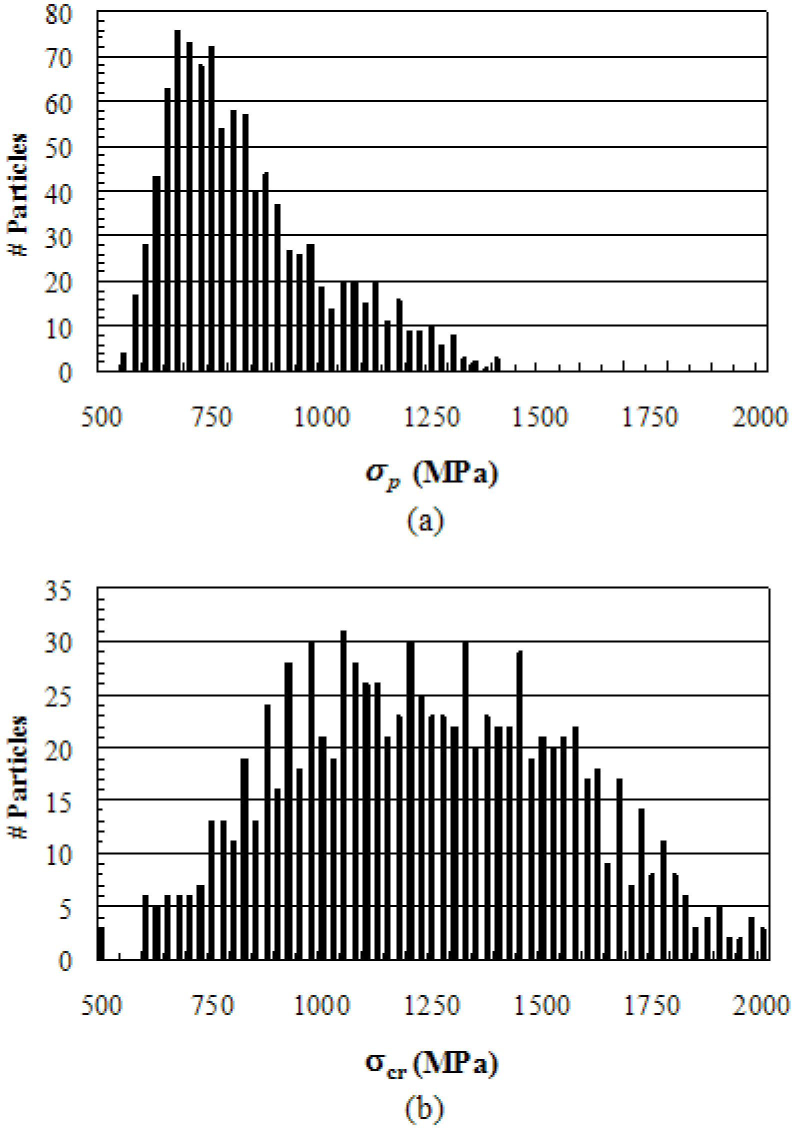

Figure 18. Histograms of (a) σ_p and (b) σ_{cr} generated from a 10,000 particle realization, with the applied strain ε_{app} equal to 1%, the fracture toughness equal to $0.14\,\mathrm{MPa}\sqrt{\mathrm{m}}$, and C equal to 0.0037.

Figure 19 shows the histogram of the difference, $\Delta\sigma = \sigma_{\mathrm{cr}} - \sigma_p$, between particle strength and stress, based on unconstrained boundary conditions. The subset of the histogram containing those particles with $\Delta\sigma < 0$ corresponds to the cracked particles. Hence, the normalized area of the particles with $\Delta\sigma < 0$ is an approximation of the probability of particle cracking. For example, for the sample shown in figure 19, the frequency is 2.3%.

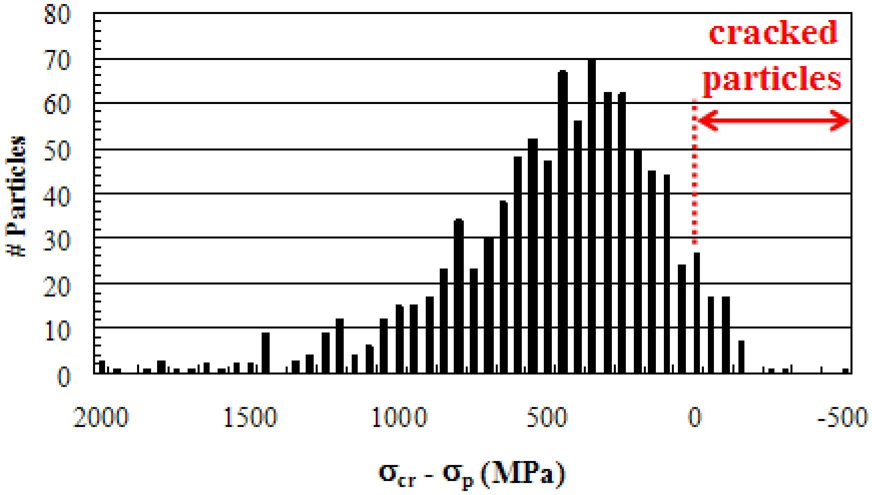

Figure 19. Histogram of the difference, $\Delta\sigma = \sigma_c - \sigma_{p\ r}$, between particle strength and stress. The subset of the histogram where $\Delta\sigma < 0$ corresponds to the cracked particles.

Twenty 10,000 particle realizations were processed for each of the boundary conditions considered for the particle stress response surface in this manner, and these produced a mean particle cracking frequency of 2.2%, with a standard deviation of 0.16% for the unconstrained boundary condition and 4.9% with a standard deviation of 0.27% for the constrained boundary conditions. This resulted in an overall mean particle cracking frequency of 3.6% with a standard deviation of 1.4%. Of the forty particle realizations that were processed, the minimum frequency found was 1.9% and the maximum was 5.3%. The two boundary conditions were considered in order to place upper and lower bounds on the range of predicted particle cracking frequency.

5. Preliminary validation

The discussion to this point has set forth a methodology for predicting Fe-bearing particle cracking in a 7075-T651 microstructure. A prediction of particle cracking can now be made for an individual particle or a distribution of particles. Two validation experiments, separate from the calibration experiment discussed in Section 3, were performed expressly for the validation of this methodology and are discussed in this section. A comparison of the particle cracking frequency observed in these experiments is made with the prediction in Section 4.2.

The DEN specimen geometry and area observed microscopically during the two validation experiments are shown in figure 20. At one edge-notch in each DEN specimen, an area of 0.75 mm^2 was observed to record the frequency of particle cracking during the application of cyclic loading. Using the cyclic load and specimen dimensions shown in figure 5, particle cracking was intermittently recorded within the observation area.

The observed particle cracking data for both DEN specimens are given in table 4. In specimen #1, there were 792 Fe-bearing particles in the observed area of which 59 particles were cracked before loading the specimen and an additional 446 particles were below the minimum size of 6 μm^2. The remaining 287 particles were tracked throughout loading and observations were recorded at the intervals given in column 1 of table 4; after reaching the first peak load, observations were recorded through 3000 load cycles at a reduced observation frequency. This was done to obtain information about particle cracking frequency versus time of occurrence within the observed area. Similarly, for specimen #2, 631 particles were observed with 42 particles cracked before loading the specimen and an additional 346 particles below the minimum size of 6 μm^2. The remaining 243 particles were tracked throughout loading at the same intervals as specimen #1. For specimen #1, 84% of the particles that eventually cracked due to cyclic loading did so by the end of the first load cycle, and 50% in specimen #2. All of the particles that would eventually crack, had cracked by 300 load cycles. The observed percentages of particles cracking due to loading, 7.3% for specimen #1 and 1.2% for specimen #2, are in good agreement with the predicted mean value of 3.6% using the response surface methodology developed herein. The combined percentage of observed particles that cracked during the first load cycle for both specimens was about 4.5%.

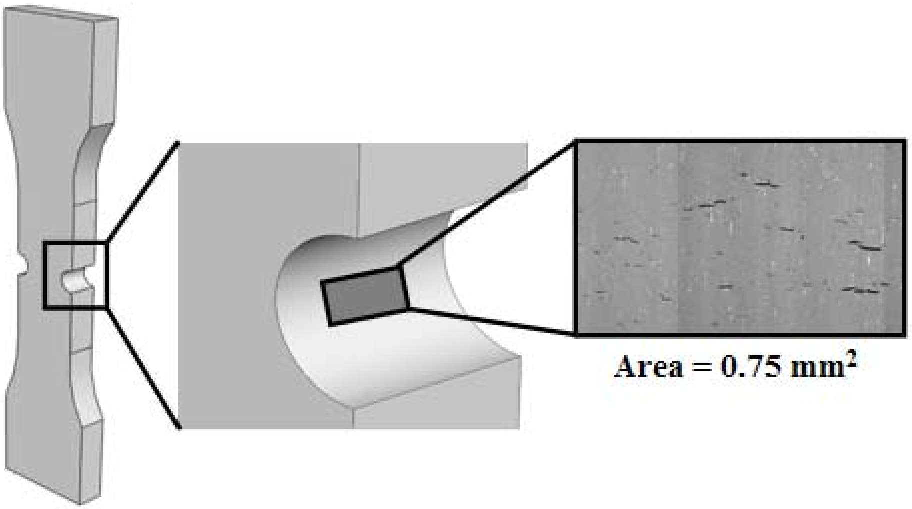

Figure 20. DEN specimen geometry showing the location and size of the area observed during the recording of particle cracking frequency for both DEN specimens.

Table 4. Accumulated percentage of Fe-bearing particles that cracked under load during the first half-cycle of loading for two DEN specimens.

Load (Cycles)	Specimen #1 (%)	Specimen #2 (%)
0.3	0.0	0.0
0.4	6.6	0.8
0.5	7.3	1.2

6. Observations and conclusions

This is the first in a series of papers on a computational simulation system capable of reproducing the mechanics and statistics found in the MSFC formation phase for 7075-T651. Throughout this series, wherever possible, statistically accurate morphologies and textures are explicitly included in all three-dimensional FE models. This paper addresses the first stage of MSFC formation: predicting the statistics of crack incubation. A mechanics-based prediction of particle cracking can now be made using distributions of particle size and aspect ratio, and grain texture. The observed statistics of incubation must be accurately predicted to simulate properly the stochastic nature of subsequent stages of MSFC formation. Future papers will address the two subsequent stages, nucleation and microstructurally small crack propagation, and provide extensive validation of the implemented criteria.

The principle adopted herein is that a particle cracks if σ_p, the particle tensile stress in the RD at point A, figure 4(a), exceeds σ_{cr}, the particle strength. A response surface was generated, for the two separate boundary conditions that bound the possible range of particle stress, using 1296 three-dimensional elasto-viscoplastic FE analyses for each condition, from which σ_p can be obtained for any combination of strain level, grain orientation, and particle aspect ratio. Seven key assumptions were made for the baseline model used in the development of the response surface:

(i) Structural models are initially stress-free;
(ii) Boundary conditions were applied for unconstrained and constrained tension in the RD;
(iii) Maximum particle tensile stress occurs:
  a. During the first load cycle;
  b. At the particle's free-surface centroid, point A;
(iv) The particle and matrix are perfectly bonded;
(v) Particle tensile stresses are accurately obtained when:
  a. Idealizing the particle as semi-ellipsoidal, and;
  b. Only the influence of the surrounding grain is considered.

The value of σ_{cr} was determined based on measured fracture toughness, particle size and an inherent flaw size material constant, *C*, Equation (20). Seven key assumptions were made for the estimation of σ_{cr}:

(i) If a particle cracks, it does so during the first cycle of loading;
(ii) σ_{cr} is a function of particle size, due to the presence of inherent particle flaws;
(iii) An inherent surface flaw exists that lies perpendicular to the loading direction, figure 14;
(iv) The inherent flaw size is much smaller than the particle size;
(v) The shape of this inherent flaw is semi-elliptical, figure 14;
(vi) a_f and b_f are proportional to a_p and b_p; and,
(vii) LEFM conditions apply.

From the development of the response surface, important findings are:

(i) The orientation of the surrounding grain causes a variability of up to 30% in σ_p;
(ii) The aspect ratio of the particle accounts for variability of up to 100%;
(iii) The combined effects of grain orientation and particle aspect ratio cause variability of up to 200%.

From the estimation of the particle tensile strength, important findings are:

(i) σ_{cr} is particularly sensitive to *C*;
(ii) The calculated mean value of *C* was 0.0037, with a standard deviation of 0.0018 for the unconstrained boundary condition, and 0.0027, with a standard deviation of 0.0013 for the constrained boundary condition.

The value of *C* was determined based on the results of one replication model. Future work will produce more replication models to improve these estimates.

The process for the prediction of particle cracking, as discussed in Section 4, can be viewed as a Boolean function that is evaluated on measured distributions to obtain the frequency of particle cracking. A series of 10,000 simulated particle realizations was processed and a frequency of particle cracking of 2.2% with a standard deviation of 0.16% was predicted for unconstrained boundary conditions and a mean of 4.9%

with a standard deviation of 0.27% for constrained boundary conditions. This resulted in an overall mean predicted particle cracking of 3.6% with a standard deviation of 1.4%. The predicted particle cracking frequency was in good agreement with the average experimentally observed particle cracking frequency of about 4.5%. Future work will determine the variation in predicted particle cracking frequency due to the variation in C and K_{IC}.

When simulating the MSFC formation phase, inserting all particles into a microstructural model for these stages is computationally intractable and physically unnecessary. The capability to predict which particles will crack can be used as a filter. This filter helps substantially reduce the number of particles that need to be included in the microstructural models and forms the basis of the future work on the subsequent stages of MSFC, crack nucleation and microstructurally small crack propagation.

Acknowledgements

This work is partially sponsored by the Defense Advanced Research Projects Agency under contract HR0011-04-C-0003. Dr. Leo Christodoulou is the DARPA Program Manager. The authors are pleased to acknowledge extensive technical discussions with members of the Northrop Grumman Structural Integrity Prognosis program, particularly Drs. Elias L. Anagnostou and John M. Papazian. The work was also partially supported by NASA through the Constellation University Institutes Program grant number NCC3-994.

References

Balay S, Buschelman K, Eijkhout V, Gropp W, Kaushik D and Knepley M 2006 *PETSc Users Manual* anl-95/11-rev. 2.3.2 ed. (DuPage County, Ill: Argonne National Laboratory)

Bowles C Q and Schive K 1973 The role of inclusions in fatigue crack initiation in an aluminum alloy *Int. J. Fat.* **9** 171-9

Brockenbrough J R, Hinkle A J, Magnusen P E and Bucci R J 1994 Microstructurally based model of fatigue and growth *NASA Conf. Publications* 3274 71-84

Campman R 2005 *Statistical analysis of second phase particles in AA 7075-T651* Master's thesis, Carnegie Mellon University

Christodoulou L and Larsen J M 2004 Using materials prognosis to maximize the utilization potential of complex mechanical systems, J. Metals **56** 15-19

Cornell Fracture Group 2007 FemLib [Online] Availabe at: http://www.cfg.cornell.edu

Curtin W A 1994 In situ fiber strengths in ceramic-matrix composites from fracture mirrors *J. Am. Ceram. Soc* **77** 1075-8

Dodhia K 2002 *Simulations of crack initiation in aluminum alloys with inclusions* Master thesis, Cornell University

Fan J, McDowell D L, Horstemeyer M F and Gall K 2001 Computational micromechanics analysis of cyclic crack-tip behavior for microstructurally small cracks in dual-phase al-si alloys *Eng. Fract. Mech.* **68** 1687-706

Fridline D 2007 personal communication, Northrop Grumman Corp., Bethpage, NY 11714

Gall K, Horstemeyer M F, Degner B W, McDowell D, and Fan J 2001 On the driving force for fatigue crack formation from inclusions and voids in a cast A356 aluminum alloy *Int. J. Fract.* **108** 207-33

Gao M, Feng C R and Wei R 1998 An analytical electron microscopy study of constituent particles in commercial 7075-t6 and 2024-t3 alloys *Metall. Mater. Trans. A* **29A** 1145-511

Gao Y X, Yi J Z, Lee P D and Lindley T C 2004 The effects of porosity on the fatigue life of cast aluminium-silicon alloys *Fat. Fract. Eng Mater Struct.* **27** 559-70

Ghosh S and Moorthy S 1998 Particle fracture simulation in non-uniform microstructures of metal-matrix composites*Acta Mater.* **46** 965-82

Gruenberg K M, Craig B A and Hillberry B M 1999 Probabilistic method for predicting the variability in fatigue behavior of 7075-T6 aluminum *AIAA* **37** 1304-10

Gungor S and Edwards L 1993 Effect of surface texture on fatigue life in a squeeze-cast 6082 alumunum-alloy *Fat. Fract. Eng. Mater. Struct.* **16** 391-403

Han C S, Wagoner R H and Barlat, F 2004 On precipitate hardening in crystal plasticity: theory *Int. J. Plast.* **20** 477-94

Harlow D G, Wang M Z and Wei R P 2006 Statistical analysis of constituent particles in 7075-T6 aluminum alloy *Metall. Mater. Trans. A* **37A** 3367-73

Hart E W 1970 Theory of dispersion hardening in metals *Acta Metall.* **20** 275-89

Heinz A and Neumann P 1991 Representation of orientation and disorientation data for cubic, hexagonal, tetragonal and orthorhombic crystals *Acta Cryst.* **A47** 780-9

Jackson P J and Basinski Z S 1967 Latent hardening and the flow stress in copper single crystals *Can. J. Phys.* **45** 707-35

Jordan, J B, Horstemeyer M F Solanki K and Xue Y 2007 Damage and stress state influence on the Bauschinger effect in aluminum alloys *Mech. Mater*. **39** 920-31

Karypis G, Schloegel K and Kumar V 2003 *PARMETIS, Parallel Graph Partitioning and Sparse Matrix Ordering Library* 3rd Ed. (University of Minnesota, Department of Computer Science and Engineering Army HPC Research Center)

Kocks U F 1970 The relation between polycrystal deformation and single crystal deformation *Metall. Trans.* **1** 1121-42

Kocks U F and Brown T J 1966 Latent hardening in aluminum *Acta Metall.* **14** 87-98

Kumar A and Dawson P R 1998 Modeling crystallographic texture evolution with finite elements over neo-eulerion orientation spaces *Comput. Methods Appl. Mech. Eng.* **153** 259-302

Kung C Y and Fine M E 1979 Fatigue crack initiation and microcrack growth in 2024-T4 and 2124-T4 aluminum alloys *Metall. Mater. Trans. A* **10A** 603-10

Lawn B 1993 *Fracture of Brittle Solids* 2nd Ed. (Cambridge University Press) p 271

Lee E H 1969 Elastic-plastic deformation at finite strain *J. App. Mech.* **36** 1-6

Lee E H 1996 Elastic-plastic waves of one-dimensional strain *Proc. 5th U.S. Nat. Congr. Appl. Mesh., ASME* 405

Li X Z, Hansen V, Gjønnes J and Wallenberg L R 1999 HREM study and structure modeling of the η' phase, the hardening precipitates in commercial Al-Zn-Mg alloys *Acta Mater.* **47** 2651-9

Matous K and Maniatty A 2004 Finite element formulation for modelling large deformations in elasto-viscoplastic polycrystals *Int. J. Numer. Meth. Eng.* **60** 2313-33

McDowell D L, Gall K, Horstemeyer M F and Fan J 2003 Microstructure-based fatigue modeling of cast A356-T6 alloy *Eng. Fract. Mech.* **70** 49-80

Mei Z and Morris J M 1993 Stress concentration due to a hemispherical surface inclusion *Int. J. Fract.* **64** 43-61

Mori T and Tanaka K 1973 Average stress in matrix and average elastic energy of materials with misfitting inclusions *Acta Metall.* **21** 571-4

Morris W L, Buck O and Marcus H L 1976 Fatigue Crack Initiation and Early Propagation in Al 2219-T851 *Metall. Trans. A* **7A** 1161-5

Morris W L 1978 The effect of intermetallic composition and microstructure on fatigue crack initiation in Al 2219-T851 *Metall. Trans. A* **9A** 1345-8

Mura T 1987 *Micromechanics of Defects in Solids* 2nd Ed. (Dordrecht, Netherlands: Kluwer) p 180-2

Murakami Y (Ed.) 1987 Stress Intensity Factors Handbook (New York: Pergamon Press)

Murakami Y and Endo M 1994 Effects of defects, inclusions and inhomogeneities on fatigue strength *Int. J. Fat.* **16** 163-82

Nan C W and Clarke D R 1995 The influence of particle size and particle fracture on the elastic/plastic eformation of metal matrix composites *Acta Mater.* **44** 3801-11

Orowan E 1948 Discussion in *Symp. on Internal Stresses in Metals and Alloys*, The Institute of Metals, London, UK 451-3

Oswald L 2003 *Effects of Microstructure on High-cycle Fatigue of an AL-ZN-MG-CU Alloy* Master's thesis, University of Pittsburgh

Pacheco P S 1997 Parallel Programing with MPI (San Fransico: Morgan Kaufmann Publishers Inc.)

Papazian J M, Anagnostou E L, Engel S, Fridline D, Hoitsma D, Madsen J, Nardiello J, Silberstein R P, Welsh G and Whiteside J B 2007a SIPS, a structural integrity prognosis system *Proc. of the IEEE Aerospace Conf.* March 3-10, 2007, T11 Z11-0901 p 1-10

Papazian J M, Anagnostou E L, Engel S, Fridline D, Hoitsma D, Madsen J, Nardiello J, Silberstein R P, Welsh G and Whiteside J B 2007b Structural integrity prognosis *Proc. of the e24th Int. Conf. on Aircraft Fatigue Symp.* Naples, Italy, May 14-18

Raju L S and Newman, Jr., I C 1979 Stress intensity factors for a wide range of semi-elliptical surface cracks in finite-thickness plates *Eng. Fract. Mech*. **11** 817-829

Riester L, Bridge R J and Breder K 1998 Characterization of vickers, berkovich, spherical and cube cornered diamond indenters by nanoindentation and sfm *Mater. Research Soc. Symp. Proc*. 45-50

Rollett A D, Campman R and Saylor D 2006 Three dimensional microstructures: statistical analysis of second phase particles in AA 7075-T651 *Materials Science Forum, Proc. Int. Conf. on Aluminum Alloys (ICAA-10),* Vancouver, Canada, 519-21

Schmitt C, Lipinski P and Berveiller M 1997 Micromechanical modeling of the elastoplastic behavior of polycrystals containing precipitates – application to hypo- and hyper-eutectoid steels *Int. J. Plast.* **13** 183-99

Shiozawa K, Tohda Y and Sun S M 1997 Crack initiation and small fatigue crack growth behavior of growth behavior of squeeze-cast Al-Si aluminum alloys *Fat. Fract. Eng. Mater. Struct.* **20** 237-47

Suresh S 1998 *Fatigue of Materials* 2nd ed. (Cambridge University Press)

Tanaka K and Mura T 1982 A theory of fatigue crack initiation at inclusions *Metall. Trans. A* **13A** 117-23

Veilleux M G 2007 *Finite element model generation of statistically accurate 7075-T651 aluminum alloy microstructures* Master's thesis, Cornell University

Xue Y, El Kadiri H, Horstemeyer M F, Jordon J B and Weiland H 2007 Micromechanisms of multistage fatigue crack growth in a high-strength aluminum alloy *Acta Mater.* **55** 1975-84